

Thermospheric Density: An Overview of Temporal and Spatial Variations

Liying Qian · Stanley C. Solomon

Received: 19 April 2011 / Accepted: 8 July 2011 / Published online: 5 August 2011
© Springer Science+Business Media B.V. 2011

Abstract Neutral density shows complicated temporal and spatial variations driven by external forcing of the thermosphere/ionosphere system, internal dynamics, and thermosphere and ionosphere coupling. Temporal variations include abrupt changes with a time scale of minutes to hours, diurnal variation, multi-day variation, solar-rotational variation, annual/semiannual variation, solar-cycle variation, and long-term trends with a time scale of decades. Spatial variations include latitudinal and longitudinal variations, as well as variation with altitude. Atmospheric drag on satellites varies strongly as a function of thermospheric mass density. Errors in estimating density cause orbit prediction error, and impact satellite operations including accurate catalog maintenance, collision avoidance for manned and unmanned space flight, and re-entry prediction. In this paper, we summarize and discuss these density variations, their magnitudes, and their forcing mechanisms, using neutral density data sets and modeling results. The neutral density data sets include neutral density observed by the accelerometers onboard the Challenging Mini-satellite Payload (CHAMP), neutral density at satellite perigees, and global-mean neutral density derived from thousands of orbiting objects. Modeling results are from the National Center for Atmospheric Research (NCAR) thermosphere-ionosphere-electrodynamics general circulation model (TIE-GCM), and from the NRLMSISE-00 empirical model.

Keywords Thermosphere neutral density · Density variation · Satellite drag · Density data · Model simulation

1 Introduction

Although the atmosphere is nearly a vacuum in the thermosphere, perturbations on satellite orbits do occur, due to the cumulative effects of variable mass density. Errors in estimating thermospheric density cause differences between predicted and actual satellite orbits.

L. Qian (✉) · S.C. Solomon
High Altitude Observatory, National Center for Atmospheric Research, Boulder, CO, USA
e-mail: lqian@ucar.edu

On short time scales, these errors reduce the fidelity of catalogs of space object orbital elements, which degrades operational tracking, collision avoidance warnings, and re-entry predictions. On longer time scales, uncertainties in long-term density variation impacts satellite design in terms of lifetime, on-board fuel, and satellite attitude control. To address these problems, observational, empirical, and numerical modeling has been developed to analyze neutral density and its variations. The region of the Earth's atmosphere where satellite drag estimations are particularly important is between 150 km and 600 km. Since neutral density decreases exponentially with height, below 150 km, satellite drag is too large for satellites to maintain orbit without propulsion, whereas above 600 km, satellite drag is usually small and has less impact on satellite operations. This 150-km to 600-km region of the atmosphere, the thermosphere/ionosphere, is highly dynamic and variable, driven by energy and momentum forcing from above and from below, and responding to its complex internal dynamics.

The primary energy input to the thermosphere/ionosphere system is solar irradiance (Knipp et al. 2004). The thermosphere absorbs solar irradiance in XUV (the soft X-ray ultra-violet, 1–30 nm), EUV (extreme ultra-violet, 30–120 nm), and FUV (far ultra-violet, 120–200 nm). Although some XUV and FUV can penetrate to the mesosphere; solar EUV is completely absorbed in the thermosphere. The solar EUV ionizes, dissociates, and excites the thermospheric constituents, creates the ionosphere, and heats the thermosphere. The second most important energy input to the thermosphere/ionosphere is geomagnetic activity resulting from the interaction between the solar wind and the Earth's magnetic field, which amplifies the magnetospheric-ionospheric current system and causes energetic particle precipitation into the atmosphere. This current system drives plasma convection in the high-latitude ionosphere, transferring energy to the thermosphere through Joule heating. Energetic particles precipitate from the magnetosphere into the underlying thermosphere/ionosphere along the Earth's magnetic field lines into the auroral region, heating the thermosphere/ionosphere mainly through ionization of thermospheric constituents. Joule heating and energetic particle precipitation can become the primary energy source for the thermosphere and ionosphere system during major geomagnetic storms (Knipp et al. 2004), and energy input from geomagnetic activity is generally more dynamic and impulsive than solar irradiance. Thermospheric neutral density perturbation due to this second major energy input was recently reviewed by Prölss (2011). In addition to these two main external forcings, the thermosphere/ionosphere is also coupled to the mesosphere energetically, dynamically, and chemically, particularly with momentum and energy forcing from various waves in the mesopause region. Furthermore, infrared cooling by radiatively active trace gases, such as CO₂, NO, CH₄, H₂O, and O₃, are also important for the energy balance of the thermosphere and mesosphere, and concentrations of these trace gases have shown long-term changes due to anthropogenic effects.

Thermospheric dynamics, mainly driven by temporal variation and spatial distribution of solar irradiance and geomagnetic forcing, redistribute composition and energy within the thermosphere. In addition, the thermosphere and ionosphere are closely coupled energetically, dynamically, and chemically. For example, the ionospheric plasma convection at high latitudes transfers energy and momentum through collisions between the plasma and the neutral species, heats the neutral atmosphere (Joule heating), and accelerates the neutral atmosphere (ion drag); the thermospheric neutral wind moves the electrically conducting plasma through the Earth's geomagnetic field and generates electric fields (dynamo). The dynamo electric field and current then affect both the neutral and plasma dynamics; and the daytime ionosphere E-layer and F1 layer are in photochemical equilibrium between production of ions through ionization and loss of ions through ion-neutral and ion-electron chemical reactions.

Variations in the external forcing, internal dynamics of the system, and coupling between the thermosphere and ionosphere, can drive complicated neutral temperature and composition variations, which changes neutral density scale height and causes complicated density variations. Neutral density varies on time scales from minutes to decades, with variations on hourly, diurnal, multi-day, 27-day solar-rotational, semiannual/annual, and solar-cycle time scales in between, and significant variation in latitude, longitude, and altitude. The purpose of this paper is to summarize and discuss these variations and their driving mechanisms, using various data sets and modeling results. In the following sections, brief descriptions of data and models will be given, followed by discussions for the temporal variations of neutral density from abrupt changes to long-term trends, and spatial variations.

2 Data and Models

Neutral density data, measured by accelerometers onboard the Challenging Minisatellite Payload (CHAMP) satellite and derived from satellite drag data, will be used throughout the paper for discussions of density variations. The National Center for Atmospheric Research (NCAR) thermosphere-ionosphere-electrodynamics general circulation model (TIE-GCM) (Roble et al. 1988; Richmond et al. 1992) was used to simulate each type of density variation for model-data comparisons. In addition, neutral density calculated by the NRLMSISE-00 empirical model (Picone et al. 2002) was also used for discussions.

2.1 CHAMP Neutral Density Data

The CHAMP satellite was launched into a near-circular orbit with an inclination of 87.3° on 15 July 2000 (Reigber et al. 2002; Lühr et al. 2004). The high inclination ensures almost complete latitudinal coverage from pole to pole. Neutral density is obtained from accelerometer measurements of non-gravitational accelerations on the CHAMP satellite (e.g., Sutton et al. 2005). The measured densities are normalized to a constant altitude of 400 km using NRLMSISE-00 (Picone et al. 2002). The temporal resolution of CHAMP neutral density is 10 seconds and the spatial resolution is 75 km, so CHAMP density data can be used to investigate spatial gradients of neutral density with good temporal resolution.

2.2 Neutral Density Data at Satellite Perigees

These neutral density data are daily averaged density obtained at satellite perigees of several low-Earth orbiting satellites from 2002 to 2006 by Bowman et al. (2004). These satellites are defunct radar calibration spheres launched by the former Soviet Union during the 1990s: Cosmos 660 (07337), Cosmos 807 (08744), Cosmos 1236 (12388), and Cosmos 1238 (12138). They are all in moderately eccentric orbits with average perigee altitudes between 380 and 430 km, and the average apogee altitude from 1300 to 1650 km. The satellite perigees scan approximately three latitude cycles and five local time cycles in a year. Errors of these density data are $\sim 2\%$ – 4% (Bowman et al. 2004).

2.3 Global-Mean Neutral Density from Satellite Drag Data

Emmert (2009) created a long-term data set of globally averaged thermosphere mass density, derived from drag data of ~ 5000 orbiting objects, for the period 1967–2009, in the altitude range from 200 to 600 km. The data have a temporal resolution of 3–6 days, a typical short-term precision of 2%, and a long-term accuracy of 5–10%.

2.4 NCAR TIE-GCM

The National Center for Atmospheric Research (NCAR) thermosphere-ionosphere-electrodynamics general circulation model (TIE-GCM) is a first principles upper atmospheric general circulation model that solves the Eulerian continuity, momentum, and energy equations for the coupled thermosphere/ionosphere system. It uses pressure surfaces as the vertical coordinate and extends in altitude from approximately 97 km to 600 km (Roble et al. 1988; Richmond et al. 1992). The default solar input is specified by the EUVAC solar proxy model (Richards et al. 1994) and solar energy deposition is calculated using the method described in Solomon and Qian (2005). In addition, solar spectral irradiance measured by the Thermosphere Ionosphere Mesosphere Energetics and Dynamics (TIMED) Solar EUV (Extreme Ultra-Violet) Experiment (SEE) (Woods et al. 2005) can be used as solar input (Qian et al. 2008, 2009), and flare spectra calculated by the Flare Irradiance Spectral Model (FISM) (Chamberlin et al. 2008) were used for flare simulations (Qian et al. 2010a). Magnetospheric energy inputs are parameterized using the 3-hour planetary Kp index. Ionospheric convection is specified by the empirical model of Heelis et al. (1982). Auroral particle precipitation and its ionization and dissociation are calculated by an analytical auroral model described by Roble and Ridley (1987). Migrating semidiurnal and diurnal tides are specified at the lower boundary using the global scale wave model (Hagan and Forbes 2002, 2003). The effect of gravity wave breaking in the mesosphere/lower thermosphere (MLT) region is included by specifying a seasonal variation of eddy diffusivity at the lower boundary that declines with altitude (Qian et al. 2009). Effects of planetary waves and nonmigrating tides are not considered in the simulations shown here.

3 Density Variations

The data sets and models described in the previous section are used in the following sections to discuss density variations. These density variations are: abrupt changes with time scales from minutes to hours, diurnal variation, multi-day variation, solar-rotational variation, annual/semiannual variation, solar-cycle variation, long-term trends with a time scale of decades, and geographic variations with latitude, longitude, and altitude.

3.1 Abrupt Changes

Abrupt changes of neutral density refer to density changes on the order of minutes to hours. Solar flares and geomagnetic storms associated with coronal mass ejections (CME) cause rapidly changing energy inputs, and thus can cause rapid changes in neutral density. Semi-empirical density models often do not adequately capture these abrupt changes in neutral density. Sudden changes seen in time series of derived ballistic coefficients for orbiting objects are often assumed to result from attitude changes, but could sometimes result from unexpected density variation. Therefore, abrupt density changes can be a major source of orbit prediction error and significantly impact satellite tracking and collision avoidance.

3.1.1 Response to Solar Flares

Solar flares can produce a large and rapid increase of solar irradiance in the X-ray and EUV ranges, causing immediate enhancement of ionization in the upper atmosphere. Most studies of terrestrial effects of solar flares have focused on the ionospheric aspects (e.g., Mitra

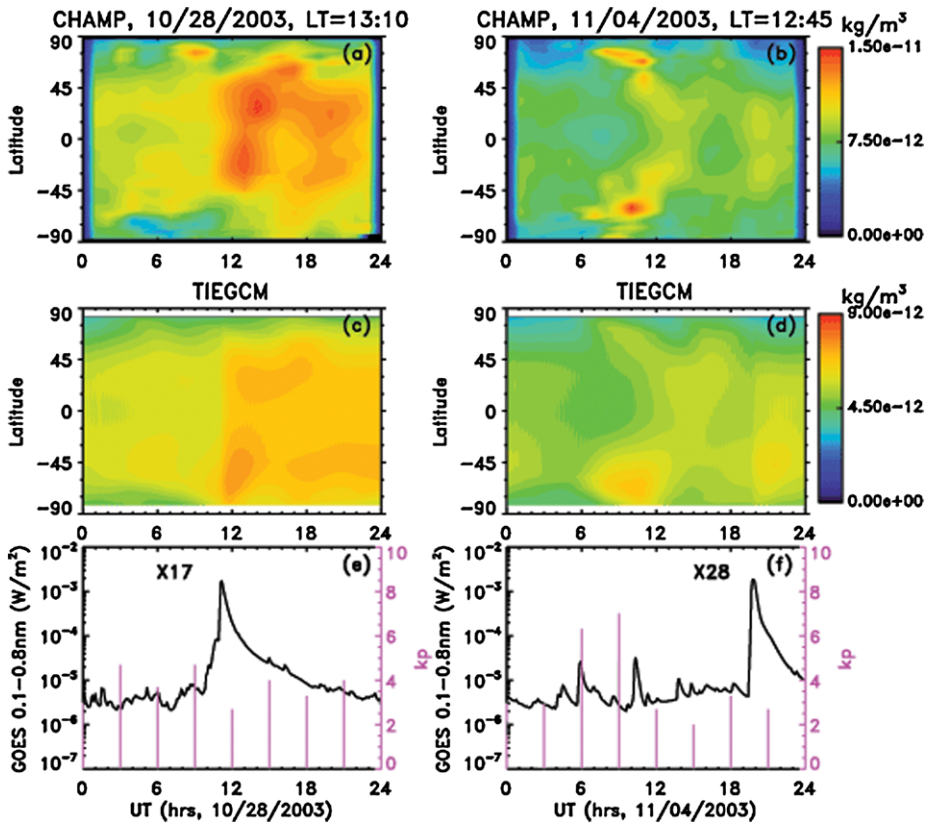


Fig. 1 Neutral density responses to an X17 flare occurred on October 28, 2003 and an X28 flare occurred on November 4, 2003. (a) Neutral density observed by CHAMP on October 28, 2003. The solar local time of CHAMP orbit was $\sim 13:10$. (b) Neutral density observed by CHAMP on November, 2003. The solar local time of CHAMP orbit was $\sim 12:45$. (c) Neutral density simulated by TIE-GCM for October 28, 2003, sampled along the CHAMP orbit. FISM flare spectra were used as solar input for the TIE-GCM. (d) Neutral density simulated by TIE-GCM for November, 2003, sampled along the CHAMP orbit. FISM flare spectra were used as solar input for the TIE-GCM; (e) GOES 0.1–0.8 nm solar irradiance and geomagnetic Kp index for October 28, 2003. (f) GOES 0.1–0.8 nm solar irradiance and geomagnetic Kp index for November 4, 2003

1974; Davies 1990; Mendillo et al. 1974; Zhang et al. 2005; Tsurutani et al. 2006), with relatively sparse research concerning the thermosphere (Sutton et al. 2005; Liu et al. 2007a; Pawlowski and Ridley 2008). The thermosphere, with its large mass and high heat capacity, is expected to be slower in responding to transient events such as solar flares. However, model simulations and observations show significant rapid density response to solar flares.

Figure 1a and 1b show neutral density at 400 km observed by the CHAMP satellite along its day-time orbit, for October 28, 2003, and November 4, 2003. Figure 1c and 1d are neutral density simulated by the TIE-GCM. Input flare spectra for the TIE-GCM were provided by the FISM (Chamberlin et al. 2008), which is based largely on data from TIMED/SEE and the X-ray monitors on the GOES satellites. TIE-GCM density was sampled along CHAMP orbits for comparison to the measured density. Figure 1e and 1f show solar flux in the wavelength range 0.1–0.8 nm measured by GOES 10, and geomagnetic Kp index. An X17 flare

occurred at 11:10 UT on October 28, 2003, and an X28 flare occurred at 19:45 UT on November 4, 2003. For the X17 flare, the sudden increase of solar XUV and EUV drove a rapid increase in density. The magnitude of density enhancement and peak response time vary with latitude. The model simulated density enhancement is somewhat weaker than the observations. On average, peak density response is on the order of 30 to 40%. The peak response time varies from ~ 1 h to ~ 3 h, depending on latitude. These results are consistent with results by Sutton et al. (2005) and Liu et al. (2007a) for the same flare. By comparison, density enhancement during the X28 flare on November 4, 2003 is much weaker, as shown in Figs. 1b and 1d. Both model simulation and observations indicate a density enhancement on the order of $\sim 10\%$. There is density enhancement earlier during the day between $\sim 6:00$ UT and $\sim 15:00$ UT, which is due to a geomagnetic disturbance, as indicated by the Ap index in Fig. 1f.

This seemingly contradictory relationship between the density response to the X28 flare and the X17 flare has to do with the spectral characteristics of the emission enhancement, which was due to their different locations on the solar disk. The X28 flare was a limb flare whereas the X17 flare occurred near the solar disk center. Qian et al. (2010a) investigated how the location of a flare on the solar disk affects thermosphere and ionosphere responses, finding that flare enhancements of XUV and EUV spectral irradiance are affected by disk location. Most emission lines in the XUV region (~ 0.1 to ~ 25 nm) are optically thin, and are weakly dependent on the location of a flare, but in the EUV region (~ 25 to ~ 120 nm), many important lines and continua are optically thick, so enhancements are weaker for flares located near the solar limb, due to absorption by the solar atmosphere. Consequently, in the E region ionosphere, where solar XUV dominates ionization, flare location does not affect thermosphere and ionosphere responses. However, flare response of neutral density in the upper thermosphere is 2 to 3 times stronger for a disk-center flare than for a limb flare, due to the fact that neutral gas heating through ionization by solar EUV is dominant in the 150–300 km region. Zhang et al. (2011) conducted statistical analysis and found that at the same X-ray class, flares near the solar disc center have much larger effects on the ionospheric TEC than those near the solar limb region.

The initial flare response occurs on the sunlit side of the Earth, so flare response is best observed on the dayside at low- to mid-latitudes. However, intense dayside heating can launch nightward propagating gravity waves that transport energy efficiently to the nightside at velocities near the local sound speed plus the bulk wind velocity in a matter of hours, with flare response occurring on the night side about 4 to 5 hours later. This nightside density enhancement was observed by CHAMP and simulated by upper atmospheric models (Pawłowski and Ridley 2008; Qian et al. 2010a).

Many questions concerning flare effects remain, for example, how other flare characteristics, such as flare rise time and decay time, affect thermosphere responses, whether latitudinal dependence of amplitude and density response time are determined by solar zenith angle, and how the thermosphere and ionosphere are coupled or decoupled in the phases of response and recovery (Qian et al. 2011). Combined modeling and data studies are needed to answer these questions and understand the underlying physical mechanisms.

3.1.2 Response to Geomagnetic Storms

Geomagnetic storms addressed in this section are those caused by CMEs, which occur as a result of a sudden increase of dynamic pressure in the solar wind, and changes in strength and orientation of the interplanetary magnetic field (IMF). These geomagnetic storms generate rapidly changing energy inputs, and occur predominantly at higher levels of solar activity. Solar wind energy is transferred from the magnetosphere to the ionosphere and the

thermosphere through plasma convection and energetic particle precipitation; both are high latitude phenomena. The increased plasma convection causes a substantial increase in Joule heating, and energetic particle precipitation heats the thermosphere and the ionosphere in the auroral region through ionization, dissociation, and excitation of neutral constituents, mainly at E-layer altitudes. Joule heating usually dominates particle heating during large geomagnetic storms (Wilson et al. 2006). The initial storm response occurs at high latitudes, and neutral density responses to storms are best observed at high latitudes (e.g., Liu and Lühr 2005). The thermosphere responds to the heating with increased temperature, intensified large-scale circulation, redistribution of composition, and increased neutral mass density. The localized heating can then excite gravity waves at high latitude (e.g., Bruinsma et al. 2006). Disturbances at high latitude are then propagated to lower latitudes by large-scale circulation and waves, causing perturbation at lower latitudes with several hours delay (Bruinsma et al. 2006). As a result, geomagnetic storm-driven increases of density become a global phenomenon.

Neutral density response to a geomagnetic disturbance that occurred on November 4, 2003, is evident in Fig. 1b, 1d, and 1f. The 3-hour K_p index was 6–7 from 6:00–9:00 UT, and the neutral density was enhanced between ~6:00 and ~15:00 UT. Neutral density increased rapidly at high latitude, responding to the disturbance, and this density enhancement moved toward lower latitudes during the next several hours. The density enhancement was on the order of ~50%. Geomagnetic storms can last for several days. During the 2003 “Halloween storm” of October 28–November 4, (day 301–308) of 2003, the K_p index remained high for almost three days. Figure 2a and 2b show neutral density at perigees of satellites #12388 and #12138 from 2003270 to 2003350 (September 27, 2003–December 16, 2003), the period surrounding this storm, derived from satellite drag and simulated by the TIE-GCM. Figure 2c shows the daily A_p index for this period. These neutral density data are daily averaged density at the satellite perigees. As mentioned earlier, these satellites have moderately eccentric orbits with perigees between 380 km and 430 km and apogees near 1500 km. The TIE-GCM simulated neutral density was sampled at perigee local time, altitude, and latitude for comparison to the data. We would point out that the altitude, latitude, and local time of the perigees changed with time, which would change neutral density. However, this change of density is gradual compared to the impulsive change due to geomagnetic activity. Figure 2 shows the direct correspondences of each impulsive change in the line plot of the neutral density to the line plot of A_p index. This clearly demonstrates how geomagnetic forcing drives impulsive variation in neutral density. The “Halloween storm” caused neutral density enhancement on the order of 100 to 200%. The different morphology of neutral density for the two satellites following the “Halloween storm” is due to the changes of altitude, local time, and latitude at the perigees. Specifically, the perigee of satellite #12388 increased from ~390 km to ~415 km and the local time at perigee progressed from near local noon to night time, consequently, neutral density was low after the storm. By contrast, the perigee of satellite #12138 decreased from ~425 km to ~395 km and the local time at perigee progressed from night time to around local noon, therefore, overall neutral density remained high after the storm.

As with the response of neutral density to flares, the characteristics of an individual geomagnetic storm, such as the orientation, strength, and variability of the interplanetary magnetic field, and the solar wind speed and density, affect the magnitude, temporal, and spatial features of the resulting density changes (e.g., Liu et al. 2010, 2011). The level of solar activity, season, and UT at storm onset also has a significant effect (Burns et al. 2004), due largely to variations in ionospheric conductivity. Response timing and duration also vary strongly with altitude (Wang et al. 2008). The altitude distribution of Joule heating is very important

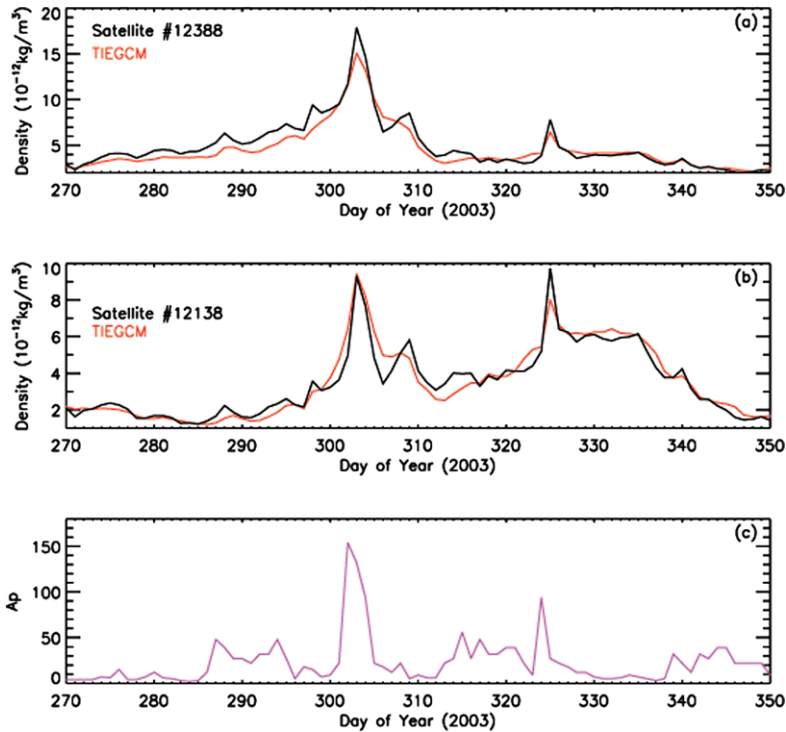


Fig. 2 The impulsive changes of neutral density responding to the geomagnetic storms in November, 2003. **(a)** Neutral density at the perigees of satellite #12388 from 2003270 to 2003350 (September 27, 2003–December 16, 2003). *Black*: derived from satellite drag; *red*: simulated by TIE-GCM. **(b)** Neutral density at the perigees of satellite #12138 from 2003270 to 2003350 (September 27, 2003–December 16, 2003). *Black*: derived from satellite drag; *red*: simulated by TIE-GCM. **(c)** Corresponding geomagnetic Ap index during the period. *Note*: the altitude, latitude, and local time of the satellite perigees changed with time through the period. However, these density changes are gradual compared to the impulsive changes of neutral density directly corresponding to the impulsive changes in Ap index shown in this figure

to thermosphere and ionosphere responses. Compared to lower-altitude Joule heating, high-altitude heating produces a strong, immediate density response that rapidly decays when the heating ends (Deng et al. 2010). More investigation is needed to quantify the distribution of magnetospheric energy inputs to the thermosphere/ionosphere system during a storm, and how the energy partitioning and ionosphere conditions determine neutral density response.

3.2 Diurnal Variation

Since solar irradiance is the primary energy source for the thermosphere, thermospheric density exhibits large diurnal variation. Müller et al. (2009) conducted statistical analysis to CHAMP neutral density at low latitude (± 30 geographical latitude) and found that the ratio between the density on the dayside (10:30–16:30 LT) and night side (22:30–04:30 LT) is 2 ± 0.1 during geomagnetic quiet time, nearly independent of solar activity level and season. Figure 3a shows neutral density from day 270 to day 274 of 2007 observed by CHAMP along CHAMP's ascending orbit ($\sim 13:00$ LT) and descending orbit ($\sim 01:00$ LT). Figure 3c and 3d shows TIE-GCM simulated neutral density sampled along CHAMP's as-

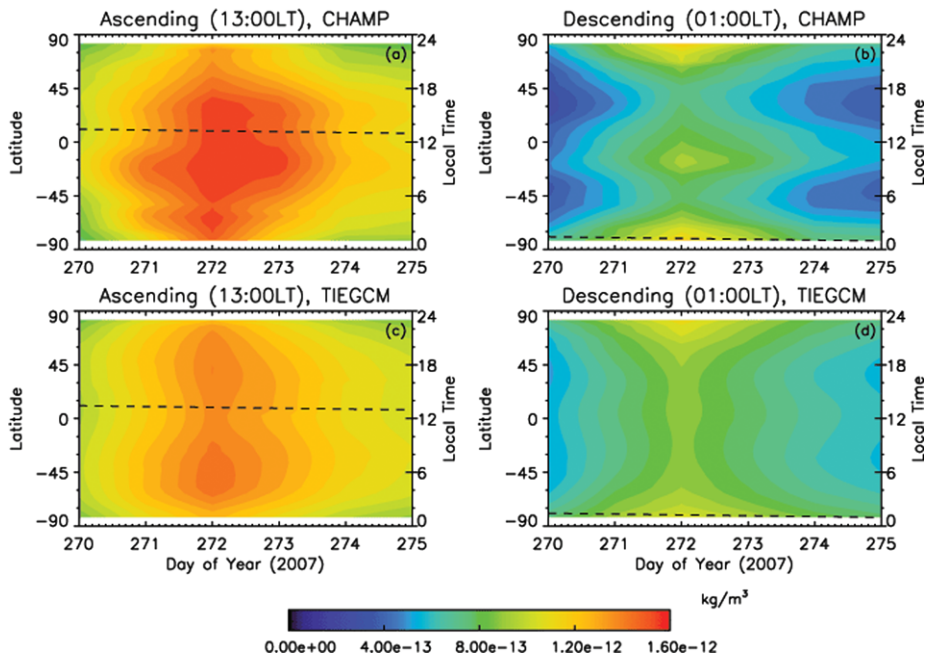


Fig. 3 Diurnal variation of neutral density. **(a)** Day time neutral density along CHAMP ascending phase of the orbit from day 270 to day 274, at $\sim 13:00\text{LT}$, observed by CHAMP. The *black dashed lines* shows local time of the ascending phase for each day. **(b)** Night time neutral density along CHAMP descending phase of the orbit from day 270 to day 274, at $\sim 01:00\text{LT}$, observed by CHAMP. The *black dashed lines* shows local time of the descending phase for each day. **(c)** Day time neutral density along CHAMP ascending phase of the orbit from day 270 to day 274, at $\sim 13:00\text{LT}$, simulated by TIE-GCM. The *black dashed lines* shows local time of the ascending phase for each day. **(d)** Night time neutral density along CHAMP descending phase of the orbit from day 270 to day 274, at $\sim 01:00\text{LT}$, simulated by TIE-GCM. The *black dashed lines* shows local time of the descending phase for each day

ending and descending orbits, respectively. The observed and simulated density difference between these two local times is $\sim 80\text{--}100\%$.

These diurnal variations of neutral density in the upper thermosphere (around 400 km) are mainly caused by in-situ diurnal variation of solar irradiance. In the lower thermosphere, diurnal variation can be modulated by tides (e.g., Hagan et al. 1997; Forbes et al. 2003). These tides are originated in the troposphere and propagate upward into the lower thermosphere. Recent analysis of CHAMP and GRACE neutral density suggests that effects of these tides can reach the upper thermosphere (Forbes et al. 2009). Therefore, diurnal variation of neutral density, even in the upper thermosphere, may include contribution from the lower atmosphere tides, however, this contribution should be small compared to the contribution by the in-situ solar irradiance.

3.3 Multi-day Variation

Multi-day variations refer to density variation with a periodicity at sub-harmonics of the solar rotation period. The multi-day density variation is primarily caused by recurrent geomagnetic forcing. Compared to geomagnetic storms driven by CMEs discussed in Sect. 3.1, this recurrent geomagnetic forcing is at low to moderate geomagnetic activity levels associ-

ated with co-rotating interaction regions (CIR) (Tsurutani et al. 1995), that occur predominantly in the declining and minimum phases of a solar cycle. Multi-day periodicities at sub-harmonics of the solar rotation period (~ 9 day, ~ 7 day, ~ 5 day) have been observed in the interplanetary magnetic field and solar wind speed during the declining phase of solar cycle 23, related to the distribution of coronal holes on the Sun, where high-speed solar wind streams originate (Temmer et al. 2007). Consequently, these periodicities are also seen in auroral precipitation and various geomagnetic activity indices (Emery et al. 2009) as the solar wind interacts with the Earth's magnetosphere. The resulting periodicities in geomagnetic activity affect the thermosphere and ionosphere through auroral particle precipitation and Joule heating. Lei et al. (2008) found a strong (~ 30 – 50%) 9-day periodicity in neutral density observed by CHAMP during 2005.

Qian et al. (2010b) assessed modeling capability in simulating thermospheric response to this recurrent geomagnetic forcing, and investigated vertical variation of the multi-day variation. They found that the simulated multi-day variation agrees well with measurements. The multi-day oscillation of density is globally distributed in the upper thermosphere, but restricted to high latitudes in the lower thermosphere. The upper thermosphere density variation exhibits less latitudinal dependence than the temperature variation, because the latitudinal dependence of composition compensates for the temperature effect by reducing the density scale height. The differences between latitudinal variations of neutral density, neutral temperature, and composition will be further discussed in Sect. 3.8.

Figure 4a shows neutral density at 400 km from day 240 to day 300 of 2007, observed by CHAMP along its ascending orbit, and Fig. 4b shows TIE-GCM simulated density sampled along the CHAMP's ascending orbit. The local time changes from $\sim 16:00$ to $\sim 10:45$ during the 60 days. Figure 4c shows the corresponding F10.7 and Ap indices. Figure 4 clearly shows the observed and simulated multi-day variations of neutral density that are globally distributed at this altitude, and demonstrates the correlation between multi-day density variation and multi-day variation in Ap index.

Forcing from the lower atmosphere can also cause multi-day density variation. Although most planetary waves dissipate in the stratosphere and lower mesosphere, planetary waves with periods of 2, 5, 10, and 16 days have been observed in the mesosphere and lower thermosphere region (e.g., Jacobi et al. 1998; Clark et al. 2002). These waves, when present, may also contribute to multi-day periodicities observed in the thermosphere and ionosphere.

3.4 Solar-Rotational Variation

Solar-rotational variation of thermospheric density is caused by the appearance and disappearance of the Sun's active regions as the Sun rotates in an average 27-day period. The active regions can be seen through the Sun's hydrogen image that features bright regions identified as solar plages. Plages are localized regions with intense magnetic activities that are usually associated with sunspots. Plages are distributed non-uniformly and appear primarily within 30° latitude on each side of the equator of the Sun. These features usually appear and disappear over a period of several months. As the Sun rotates with an approximate 27-day period, the non-uniform active regions emerge and vanish to the Earth's atmosphere. This produces a rotational variability in solar irradiance with a magnitude proportional to the contrast and fractional areas between active regions and quiet regions, as well as a strong 27-day periodicity in geomagnetic activity. Since the Sun is very active under solar maximum conditions, solar-rotational variation is larger under solar maximum conditions compared to solar minimum conditions. Figure 5a and 5b shows global-mean neutral density at 400 km, derived from satellite drag (Emmert 2009) and simulated by the

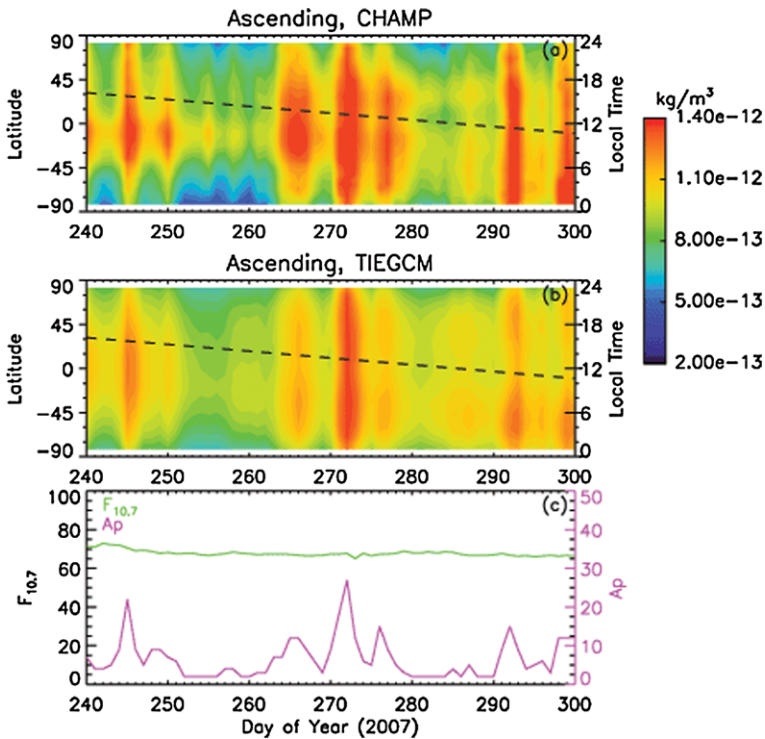


Fig. 4 Multi-day variation of neutral density. (a) Neutral density along CHAMP ascending phase of the orbit from day 240 to day 299 of 2007, observed by CHAMP. The black dashed lines shows local time of the ascending phase for each day. (b) Neutral density along CHAMP ascending phase of the orbit from day 240 to day 299 of 2007, simulated by TIE-GCM. (c) Corresponding F10.7 index Ap indices

TIE-GCM for 2003 (high solar activity) and 2008 (solar minimum), respectively. Figure 5c and 5d show the corresponding F10.7 and Ap indices for these two years. Solar-rotational variation of solar irradiance is strong in 2003 but very weak for 2008, as seen in the F10.7 index (Fig. 5c, 5d). Solar-rotational variations of neutral density are evident in the data and modeling results, and often exceed 100% for 2003. By comparison, solar-rotational variation is very minor during 2008; density during this year, a solar minimum year, exhibits a predominantly multi-day variation, primarily caused by the multi-day variation in geomagnetic activity, as we discussed in Sect. 3.3.

3.5 Annual/Semiannual Variation

Thermospheric mass density and composition exhibit a strong seasonal variation, with maxima near the equinoxes, a primary minimum during northern hemisphere summer, and a secondary minimum during southern hemisphere summer. The annual thermospheric density variation was first observed by Paetzold and Zschörner (1961) through analysis of satellite drag data. They found that neutral density has a minimum from May to August and a broad maximum during the rest of the year with a secondary minimum near January. The magnitude of the annual minimum to maximum variation is more than 100%. Using harmonic analysis, they further found that the annual variation is a semiannual variation superimposed

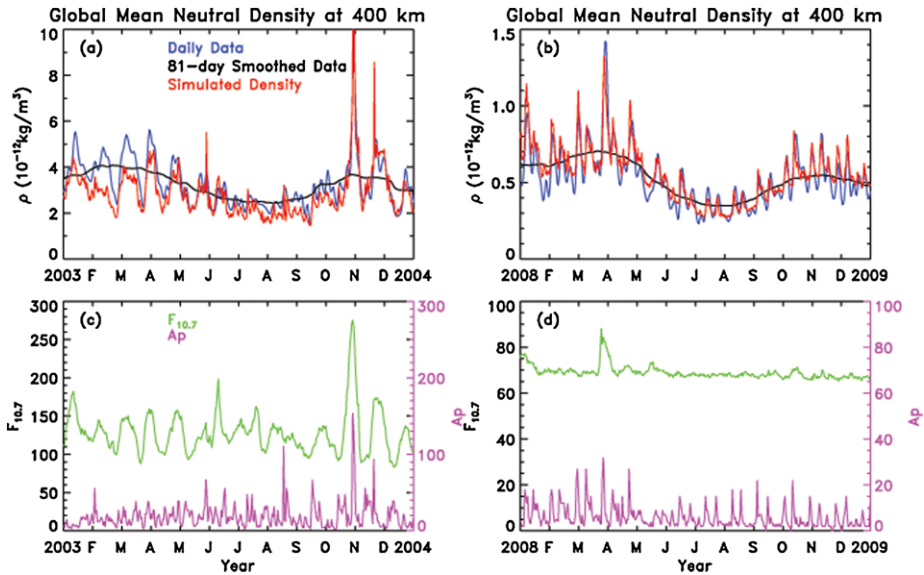


Fig. 5 Solar-rotational and annual/semiannual variations of neutral density. (a) Global-mean neutral density at 400 km for 2003. *Blue*: daily density data derived from satellite drag; *black*: 81-day running mean of the daily density data; *red*: daily density simulated by TIE-GCM. (b) Global-mean neutral density at 400 km for 2008. *Blue*: daily density data derived from satellite drag; *black*: 81-day running mean of the daily density data; *red*: daily density simulated by TIE-GCM. (c) F10.7 and Ap indices for 2003. (d) F10.7 and Ap indices for 2008

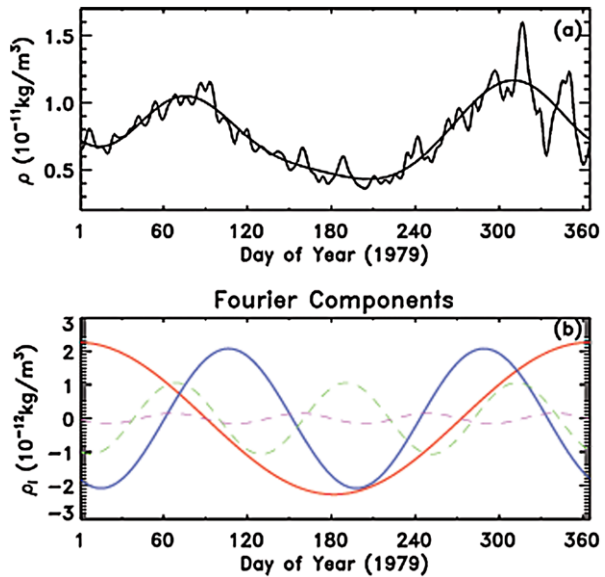
on an annual variation, and the ratio of the amplitude of the annual to semiannual variation is 3:2.

Figure 6a shows global-mean neutral density at 400 km for 1979 derived from satellite drag data (Emmert 2009). Figure 6b shows Fourier decomposition of the density from 1 to 4 cycles per year. It is clear that on seasonal scale, main components of neutral density variation are annual and semiannual variation; the amplitude from annual minimum to annual maximum is $\sim 140\%$, and the annual amplitude and semi-annual amplitude are comparable, on the order of $\sim 100\%$.

Jacchia (1965) represented annual/semiannual density variation with temperature functions in his 1965 thermospheric empirical density model (J65). Jacchia (1971) then revised the J65 model approach, and represented annual/semiannual variation in the density formula with amplitude as a function of height. The MSIS series of models (Hedin 1991; Picone et al. 2002) represent annual/semiannual density variation with a combined contribution from temperature and composition variation. The composition function is imposed at 120 km and propagates to the upper thermosphere through molecular diffusion.

Bowman (2004) investigated the annual/semiannual density variation by analyzing drag data from 1970–2002 for 13 satellites with perigee heights between 200 km and 1100 km. He found that both the phase and amplitude of the annual/semiannual density variation change from year to year, with more complicated phase variation under high solar activity conditions. The amplitude increases with altitude from 200 km to 800 km and then declines at higher altitudes. The amplitude (yearly minimum to yearly maximum) can change from year to year from 30% to 250%, depending on solar activity and altitude. Bowman (2004) developed new empirical equations of annual/semiannual density variation based on the equation

Fig. 6 Annual/semiannual variation of neutral density at 400 km. **(a)** Global-mean neutral density at 400 km for 1979, derived from satellite drag. The *smooth line* is Fourier fit of the data. **(b)** Components of Fourier decomposition of the neutral density data. *Red*: the annual component; *blue*: the semi-annual component; *green*: the three-cycle per year component; *magenta*: the four-cycle per year component



used in Jacchia71 model (Jacchia 1971); the amplitude and phase functions of the equation were based on data fitting and used F10.7 index. Bowman et al. (2007) updated the J71 empirical density model to Jacchia-Bowman 2006 model (JB2006), including the new annual/semiannual formula. Bowman et al. (2008) further investigated annual/semiannual density variation and found that the phase and amplitude of annual/semiannual variation can be better parameterized using combined solar indices S_{10} and M_{10} as opposed to using F10.7 index alone. Bowman et al. (2008) used this new parameterization of annual/semiannual variation in the JB2008 model, the revised version of JB2006.

Emmert and Picone (2010) developed an empirical Global Average Mass Density Model (GAMDM) using the global neutral density data set of Emmert (2009). The model represents density as a function of the F10.7 index, the day of year, and the Kp geomagnetic activity index. The model has two terms for annual/semiannual variation that include a core seasonal term and an F10.7 modulated seasonal term. They found that the amplitudes of the annual and semiannual harmonics increase with height and F10.7; the inter-annual variability of the amplitudes is comparable to their increase from solar minimum to solar maximum; and at 400 km, the average amplitude of the annual variation is $9.8 \pm 1.6\%$ at solar minimum and $15.1 \pm 1.8\%$ at solar maximum. The corresponding semiannual amplitudes are $16.4 \pm 1.1\%$ and $21.0 \pm 1.2\%$. We would note that these amplitudes are the values between the extremes and the mean values, therefore, we should double these amplitudes in comparison with the peak-to-peak amplitudes of Bowman (2004). The peak-to-peak amplitudes of Emmert and Picone (2010) are consistent with the amplitude of Bowman (2004) for solar minimum conditions, but are considerably smaller for solar maximum conditions.

Müller et al. (2009) examined the annual/semiannual variation of neutral density using CHAMP data. They used data at the low latitude, at fixed local time intervals (10:30–16:30 LT and 22:30–04:30 LT), and under geomagnetic quiet conditions ($A_p < 15$). In addition, they normalized the data to 400 km and a fixed solar activity level ($P_{10.7} = 130$, where $P_{10.7}$ is the average of $F_{10.7}$ and 81-day average $F_{10.7}$). The purpose of this data selection was to remove the effects of various forcing on the annual/semiannual variation, such as solar and geomagnetic activity, solar zenith angle, local time, and altitude. They found that the peak

to peak amplitude of the annual/semiannual variation is 60% at $P_{10,7} = 130$, corresponding to the amplitude of Bowman (2004) for solar minimum conditions.

Empirical models can parameterize and reproduce the annual/semiannual density variation, but mechanisms for the variation are not addressed. The annual 7% variation of insolation due to variation of the Sun–Earth distance can result in an annual asymmetry, with terrestrial perihelion and hence maximum irradiance during January. However, Paetzold and Zschörner (1961) found that the resulting amplitude is too small compared to what was observed by satellite drag data. Sensitivity tests using the TIE-GCM showed that on global-average and under solar minimum conditions, the 7% variation in solar irradiance can cause a ~2%–5% annual asymmetry in neutral temperature and ~25% annual asymmetry in neutral density at 400 km. The observed annual asymmetry shown in Fig. 5b for 2008, a solar minimum year, is ~50–60%, therefore, the Sun–Earth distance alone cannot account for the observed annual asymmetry. Walterscheid (1982) suggested that there is a globally averaged temperature difference between solstice and equinox because of stronger geomagnetic activity at equinoxes than solstices due to the “Russell-McPherron effect” (Russell and McPherron 1973). This semiannual variation in geomagnetic activity can cause a small semiannual variation in neutral density (Detman 1996). Fuller-Rowell (1998) proposed the large-scale inter-hemispheric circulation as a mechanism for global semiannual density variation; the large-scale inter-hemispheric circulation acts as a “thermospheric spoon” to mix the atmosphere; since the circulation is stronger during solstice seasons, it causes a global semiannual variation in neutral density with maxima during equinox seasons and minima during solstices.

Recent model simulations (Qian et al. 2009) using the TIE-GCM indicate that these mechanisms do not fully account for the observed annual/semiannual amplitude, primarily because of the lack of a minimum during northern hemisphere summer. Qian et al. (2009) proposed forcing by the lower atmosphere as a mechanism for the annual/semiannual variation in the thermosphere: gravity wave breaking can cause a annual/semiannual variation in eddy mixing; increased eddy diffusion during northern hemisphere summer accelerates the downward transport of O to the mesopause where it recombines; composition change in the lower thermosphere affects the entire thermosphere through molecular diffusion. They derived an empirical variation of the eddy diffusion coefficient applied on a global basis to the lower boundary of the TIE-GCM (~97 km). The simulated global mean neutral density shown in Fig. 5 employed this annual/semiannual variation of eddy diffusion. The simulated neutral density agrees well with the data. Annual/semiannual density variation is evident in the observed and simulated neutral density for both the high solar activity year 2003 and the solar minimum year 2008. Amplitudes (between yearly minimum and yearly maximum) are ~60% and ~110% for 2003 and 2008, respectively. Combined data analysis using a thermosphere density data set, middle atmosphere temperature and wind data, and whole atmosphere model simulations, are needed to investigate this possible connection between the lower and upper atmosphere.

Annual/semiannual variation of neutral density is discussed again in Sect. 3.8 as it pertains to the latitudinal variation of neutral density for the four seasons. We will also discuss the annual asymmetry and possible equinoctial asymmetry components shown in the annual/semiannual variation of neutral density and composition.

3.6 Solar-Cycle Variation

Solar-cycle variation is driven by the intrinsic ~11-year variability of magnetic activity in the Sun. During a solar cycle, the plage fractional area over the solar disk varies from

0 to around 0.2. The variability of solar irradiance, mainly the EUV, drives a solar-cycle variability of neutral density in the upper thermosphere of more than an order of magnitude. Increased geomagnetic activity at solar maximum also accounts for part of this variation.

Figure 7 compares neutral density at perigee heights for satellite #12388, #07337, and #08744, derived from satellite drag data for these 3 satellites, to neutral density simulated

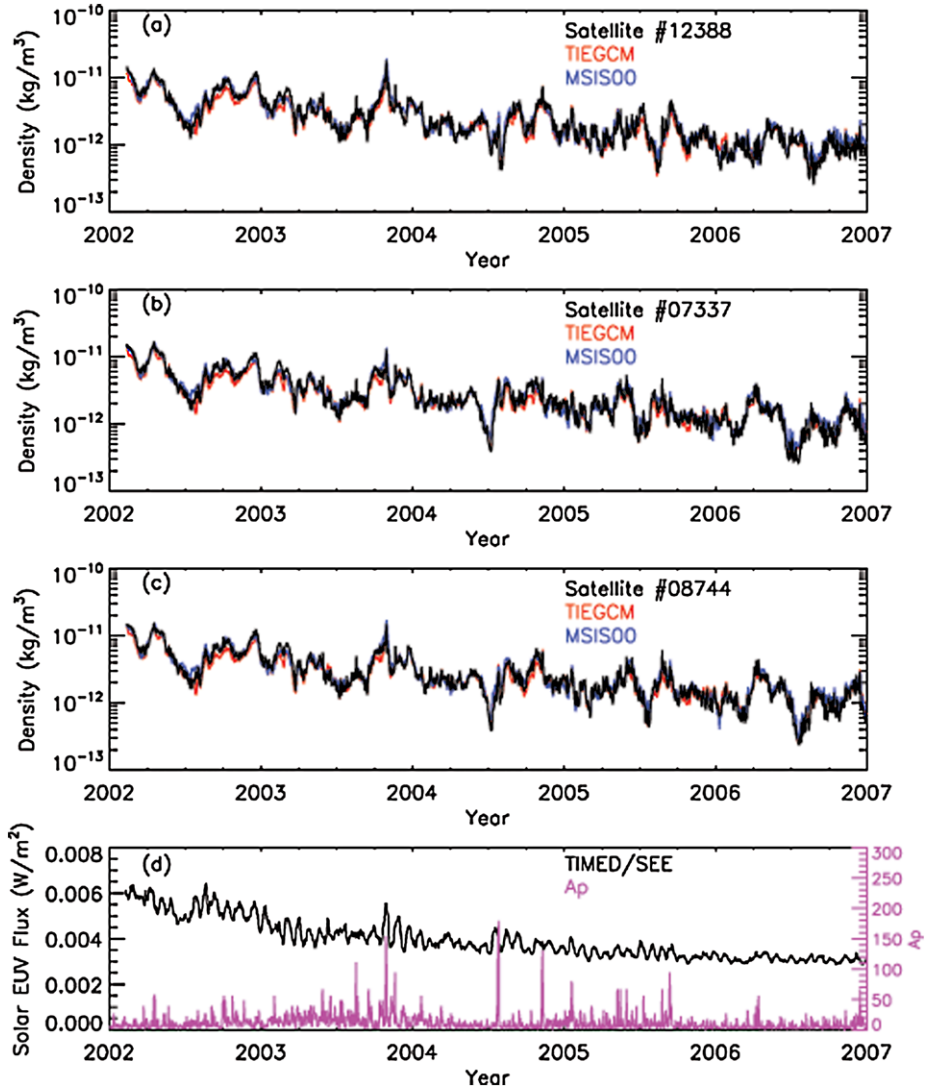


Fig. 7 Solar cycle variation of neutral density. For the simulated neutral density, TIMED/SEE measured spectral irradiance in the wavelength range 0–175 nm were used as solar input for TIE-GCM. (a) Neutral density at the perigees of satellite #12388 from 2002 to 2006. *Black*: derived from satellite drag; *red*: simulated by TIE-GCM; *blue*: calculated by MSIS00. (b) Neutral density at the perigees of satellite #07337 from 2002 to 2006. *Black*: derived from satellite drag; *red*: simulated by TIE-GCM; *blue*: calculated by MSIS00. (c) Neutral density at the perigees of satellite #08744 from 2002 to 2006. *Black*: derived from satellite drag; *red*: simulated by TIE-GCM; *blue*: calculated by MSIS00. (d) TIMED/SEE integrated solar EUV (5–105 nm) and geomagnetic Ap index from 2002 to 2006

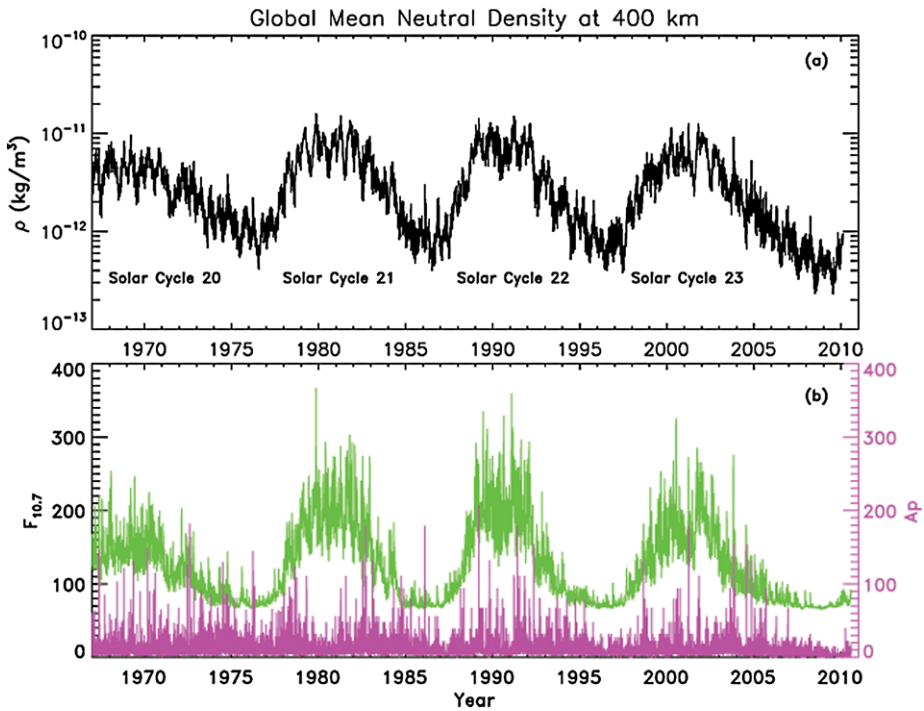


Fig. 8 Solar cycle variation and long-term trend of neutral density. (a) Global mean neutral density at 400 km derived from satellite drag data (Emmert 2009) from 1967 to 2010. (b) Corresponding $F_{10.7}$ and A_p indices

by the TIE-GCM and calculated using MSIS00, from 2002 to the beginning of 2007. Neutral density from the TIE-GCM and MSIS00 was sampled at the perigees of each satellite. In these simulations, solar spectral irradiance in the range of 0–175 nm, observed by TIMED/SEE, was used as solar input for TIE-GCM. Figure 7d shows the corresponding integrated solar EUV irradiance (5–105 nm) measured by TIMED/SEE, and the A_p index. From 2002 to the beginning of 2007, the integrated solar EUV changed from $\sim 0.006 \text{ W/m}^2$ to $\sim 0.003 \text{ W/m}^2$; and neutral density changed about one order of magnitude.

Figure 8 shows global-mean neutral density at 400 km for nearly 4 solar cycles from the density data set of Emmert (2009), as well as the corresponding $F_{10.7}$ and A_p indices. The amplitude of solar-cycle density variation for solar cycle 20 is about a factor of five; the amplitudes for solar cycles 21–23 are more than an order of magnitude. In addition, Fig. 8 demonstrates that solar irradiance is the primary forcing for the thermosphere that determines the baseline average neutral density, whereas geomagnetic forcing drives short-term variability.

3.7 Long-Term Trends

In Fig. 8, it is noticeable that neutral density at each solar minimum is lower than that at the previous solar minimum. This indicates a long-term trend of neutral density that we will discuss in this section. This long-term trend has been attributed primarily to the long-term changes of trace gases, mainly CO_2 (Laštovička et al. 2006).

Anthropogenic emissions of greenhouse gases are considered to be the primary cause of global warming in the troposphere during the past 50 years, due to the fact that these gases

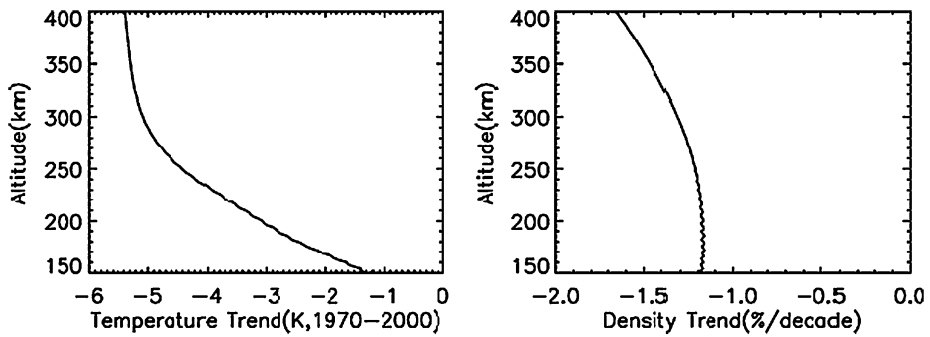


Fig. 9 Altitude profiles of long-term trends of neutral temperature and neutral density, simulated by the GLBMEAN, for the period from 1970–2000. CO₂ concentration from 1970 to 2000 observed at Mona Loa solar observatory was used as green house forcing for the model

are optically thick to outgoing infrared radiation and thus produce a heating effect. In the middle and upper atmosphere, however, greenhouse gases have an opposite, cooling effect. Greenhouse gases are optically thin to outgoing infrared radiation in the middle and upper atmosphere due to low density. Greenhouse gases absorb thermal energy through in-situ collisional excitation and then radiate to space in infrared, causing a cooling effect. Roble and Dickinson (1989) first suggested that global cooling would occur in the upper atmosphere in conjunction with global warming in the troposphere due to the long-term increase of greenhouse gas concentrations, particularly CO₂. Modeling studies by Rishbeth (1990) and Rishbeth and Roble (1992) broadened these results to the thermosphere-ionosphere system. Since the thermosphere is approximately under hydrostatic equilibrium, the height of a given pressure surface is determined by the average atmospheric temperature below. The cooling therefore results in thermal contraction of the upper atmosphere, and we may expect a significant decline in thermospheric density at fixed heights.

This long-term decreasing trend of neutral density has been observed using long-term satellite drag data (e.g., Keating et al. 2000; Emmert et al. 2004, 2008; Marcos et al. 2005). The estimated density trend at 400 km ranges from $-1.7\%/decade$ to $-3.0\%/decade$, for the past 3 to 4 decades. The density trend anti-correlates with solar activity, with about $-1\%/decade$ to $-2\%/decade$ under solar maximum conditions and about $-3\%/decade$ to $-5\%/decade$ for solar minimum conditions. In addition, the density trend increases with altitude. The solar cycle dependence is due to the relative importance of CO₂ infrared cooling and NO infrared cooling under different solar activity conditions (Qian et al. 2006). These observational findings are qualitatively consistent with modeling results by Roble and Dickinson (1989). Using CO₂ concentrations measured at Mauna Loa, Qian et al. (2006) calculated neutral density trend for the period from 1970 to 2000, and found an average density trend of $-1.7\%/decade$ at 400 km. Model simulations also showed that this density trend corresponds to a neutral temperature trend of -5.4 K for this three decades at 400 km. Figure 9 shows altitude profiles of the temperature trend and neutral density trend from 1970 to 2000, from the model simulations of Qian et al. (2006).

As mentioned earlier, this long-term decreasing trend of neutral density is discernable in the long-term density data shown in Fig. 8, as indicated by the gradual decrease of density at each solar minimum. However, as can be seen in Fig. 8, density at the minimum between solar cycles 23 and 24 is $\sim 30\%$ lower than the density at previous minimum (Emmert et al. 2010; Solomon et al. 2010), greatly exceeding the observed and modeled long-term trend. Model simulations using a global-mean version of TIE-GCM demonstrates that long-term

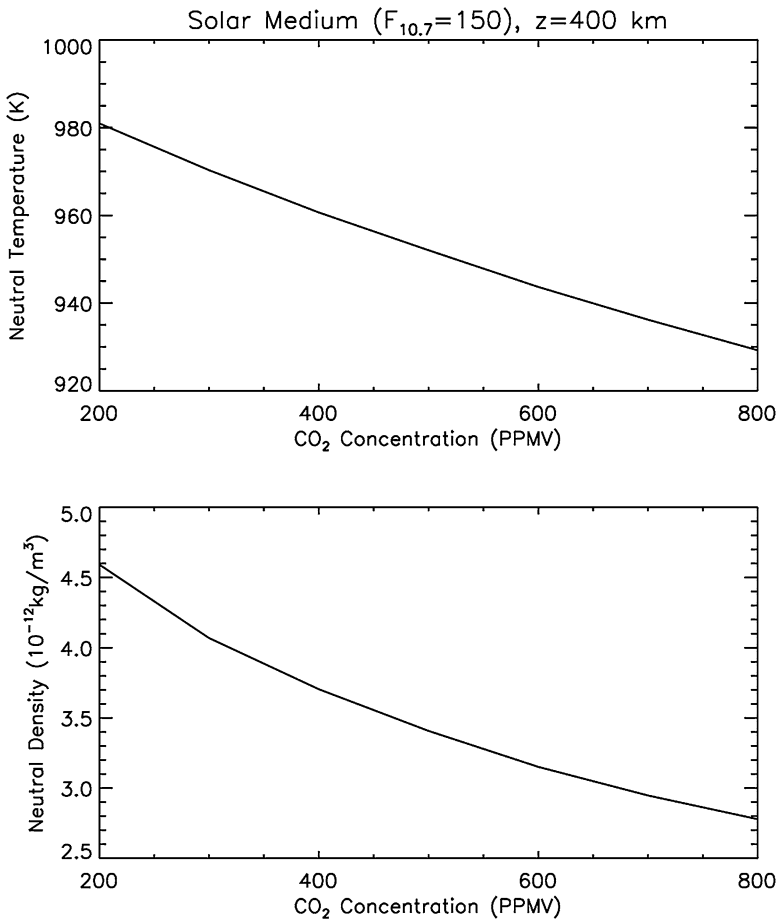


Fig. 10 Sensitivity of long-term trends of neutral temperature and neutral density to CO₂ concentration, simulated by the GLBMEAN, under solar medium condition

cooling due to CO₂ does not accelerate as CO₂ concentration increases. Figure 10 shows the simulated temperature and neutral density under solar medium ($F_{10.7} = 150$) as CO₂ concentration changes from 200 ppmv to 800 ppmv. Temperature variation with CO₂ concentration is quite linear in this large range of CO₂ concentration. Density shows only a slight non-linear relation with CO₂ concentration due to the exponential decrease of density with scale height. Therefore, the ~30% decrease of neutral density at this solar minimum is not due to accelerated global cooling. Model simulations using SOHO SEM measurements (Solomon et al. 2010) and MgII core-to-wing ratio (Solomon et al. 2011) indicated that the primary cause of the anomalous low density at solar cycle 23 minimum is anomalous low solar irradiance at this solar minimum, with geomagnetic forcing and anthropogenic long-term trend playing small but significant roles. On the other hand, statistical analysis using global total electron content derived from multiple GPS stations suggested that the anomalously low solar irradiance for solar cycle 23 minimum measured by SOHO SEM is incompatible with the total electron content observations (Lean et al. 2011).

3.8 Spatial Variation

The density variations addressed so far are variations with time. Another aspect of density variations are their spatial distribution. The total mass density is determined by the densities of major species. The spatial distribution of external forcing, together with internal dynamics and thermosphere/ionosphere coupling, determines the spatial variation of neutral density. By comparison with horizontal variation, the larger spatial variation of neutral density is usually the variation with altitude. On a global mean basis, the thermosphere is in diffusive equilibrium state; therefore, thermospheric neutral density decreases exponentially with increasing altitude, according to the diffusive equilibrium density scale height, which is determined by temperature and composition. Since the middle and upper thermosphere (above ~ 200 km) is nearly isothermal, the exponential decrease of neutral density is mainly due to the exponential decrease of the neutral species, which are in diffusive separation according to the individual molecular mass of each species. However, thermospheric large-scale circulation, as well as other processes such as nonmigrating tides from the lower atmosphere, can significantly change the spatial distributions of temperature and composition, and thus the spatial distribution of neutral density. Vertically, molecular diffusion constantly works to restore the atmosphere to a new diffusive equilibrium, and neutral density by large decreases exponentially with increasing altitude. In this section, we will discuss spatial variation at a fixed altitude, including latitudinal and longitudinal variations. The modification of diffusive equilibrium distribution of neutral density will also be discussed below.

3.8.1 Latitudinal Variation

At a fixed altitude, the number densities of atmospheric constituents are thermally and dynamically governed. The solar irradiance that reaches each hemisphere changes with season, causing different latitudinal variations of temperature in each season, as well as driving changes in inter-hemisphere circulation. This large-scale inter-hemispheric circulation, together with the high latitude circulation driven by geomagnetic activity, transports lighter species to different latitudes and thus causes latitudinal variation of composition. Latitudinal variations of neutral temperature and composition then determine the latitudinal variation of neutral density. In addition, the latitudinal variation of neutral density may also be affected by thermosphere and ionosphere coupling through mechanisms such as ion drag and chemical heating (Liu et al. 2007b). Figure 11 shows latitudinal distributions of zonal-average neutral density, temperature, major species number densities at 350 km, under solar minimum conditions, for the two solstices and two equinoxes, simulated by TIE-GCM. At the solstices, neutral density (Fig. 11a) increases from the winter pole to the summer pole with amplitude $\sim 40\%$; at equinoxes, the density exhibits little latitudinal variations. The large latitudinal gradient of neutral density at solstices and small latitudinal gradient of neutral density at equinoxes are consistent with the overall latitudinal distribution of neutral density observed by CHAMP (Liu et al. 2007b). However, Liu et al. (2007b) found the anomalous latitudinal variation of neutral density, the “equatorial mass anomaly” (EMA) in CHAMP density, with neutral mass density showing a dip at the magnetic equator and two crests on each side. This EMA feature is prominent during equinoxes, under high solar activity, and during 11:00LT–16:00LT. They suggested that the EMA was linked to the equatorial ionization anomaly (EIA) through neutral-ion coupling. The TIE-GCM simulated neutral density in Fig. 11a does not show the EMA feature. This is probably due to the fact that the model simulation was conducted for solar minimum conditions. In addition, Fig. 11a shows zonal-mean neutral density, which could also contribute to the lack of the EMA feature. Figure 11b

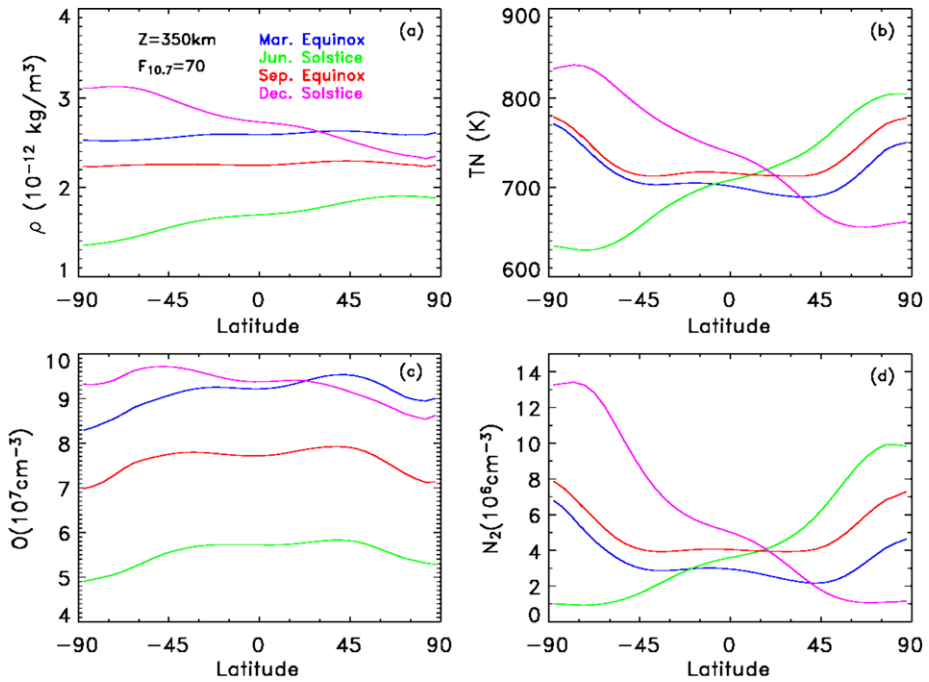


Fig. 11 Latitudinal variations of zonal-mean neutral density, neutral temperature, O number density, and N_2 number density at 350 km at equinoxes and solstices, under solar minimum and geomagnetic quiet conditions, simulated by TIE-GCM

shows latitudinal variation of zonal-mean temperature for each season. It is straightforward that temperature increases from the winter hemisphere toward the summer hemisphere. The temperature near summer pole is approximately 27% higher than near the winter pole. During equinoxes, temperature shows small latitudinal variation except at high latitudes where heating by geomagnetic activities contributes to higher temperatures in the regions.

There is a distinct difference in density annual variation (variation between the two solstices) between the Arctic and the Antarctic; the density annual variation in the southern hemisphere is much larger than that in the north (Fig. 11a). The explanation can be found by investigating the change of the Sun–Earth distance in a year. At June solstice, when the Arctic circle north of 66.5°N has 24 hours of daylight, the Earth is near the aphelion point where it is farthest from the Sun. At the December solstice, when the Arctic circle is having 24 hours nighttime, the Earth is near the perihelion point where it is closest to the Sun. This means that for the Arctic circle, the variation in insolation caused by the Sun–Earth distance is opposite to the annual variation, and thus partially cancels the annual temperature difference. Consequently, the annual temperature variation in the Arctic circle is smaller (~150 K) than that in the Antarctic circle (~200 K) (Fig. 11b). The smaller annual variation in density in the Arctic circle reflects the reduction in temperature annual variation in the region.

Figure 11c and 11d show the latitudinal distribution of the number densities of the two major species, O and N_2 . There are two distinct features in O and N_2 latitudinal variations: (1) High latitude heating due to geomagnetic activity enhances N_2 number density whereas it decrease O number density at this fixed altitude (350 km); (2) O number density is nearly

same in the winter and summer hemispheres whereas N_2 number density shows an even larger latitudinal gradient from the winter hemisphere to the summer hemisphere, compared to the temperature. This is because internal dynamics transport lighter species O (lighter than mean molecular weight) differently compared to the heavier species N_2 (heavier than mean molecular weight). There are two types of vertical motions; one is the thermal expansion and contraction and the other is due to horizontal divergence and convergence. Thermal expansion and contraction result in the rise and fall of a fixed pressure surface. In the process of expansion and contraction, different species move at the same speed, and therefore, thermal expansion and contraction does not change composition at a fixed pressure surface; Vertical motion associated with horizontal divergence and convergence, however, accumulates heavier species in the heated area but transports lighter species to the colder area. This is due to the fact that this type of closed circulation moves air parcels relative to a fixed pressure surface; energy is transported from the heated area to the colder area through adiabatic cooling in the upwelling and adiabatic heating in the downwelling. There is a return flow at lower altitude from the colder area to the heated area. Since density decreases with increasing altitude, by continuity of mass, the return flow is much slower than the flow at the greater altitude. Horizontally, due to the large difference in the speed of the two flows, lighter species that have larger scale height than the mean scale height will be effectively transported from the heated area to the colder area. The opposite is true for heavier species; the heavier species will accumulate in the heated area. Vertically, a heavier species, having smaller scale height than the mean scale height, is more abundant in the lower altitudes. The upward motion will increase its mixing ratio at higher altitude but decrease the mixing ratio of lighter species. The combined effect of thermal expansion/contraction and circulations determines the different latitudinal gradients of O and N_2 number densities shown in Fig. 11c and 11d. It is important to note that the transportation of lighter species from the summer hemisphere to the winter hemisphere by the inter-hemispheric large circulation is the mechanism of the winter anomaly (or winter bulge). Detection of winter Helium bulge by satellite drag observations (e.g., Keating and Prior 1968) and mass spectrometer data (e.g., Reber et al. 1968) revealed the winter anomaly phenomenon. Helium is considered as a minor species and is not included in the TIE-GCM. However, Helium can become a major species at ~ 500 km, especially in the Helium bulge in the mid- and high latitudes in the winter hemisphere, during solar minimum years.

It is important to point out that Fig. 11a again demonstrates the annual/semiannual variation of neutral density that we discussed in Sect. 3.5. Neutral density near June solstice is lower than the December solstice, and this annual asymmetry of neutral density is $\sim 70\%$ in this simulation which is under solar minimum condition, consistent with various observations (Bowman 2004; Müller et al. 2009; Emmert and Picone 2010). Neutral density also shows asymmetry between the two equinoxes (Fig. 11a). In this simulation with constant solar minimum forcing, neutral density near March equinox is higher than the September equinox by $\sim 14\%$. This equinoctial asymmetry, with neutral density near March equinox being higher than that near the September equinox, is also observed by the CHAMP (Liu et al. 2007b; Müller et al. 2009). Furthermore, O number density shows similar annual/semiannual variations compared to the neutral density (Figs. 11a, 11c).

3.8.2 Longitudinal Variation

In order to show longitudinal variation of neutral density, we simulated neutral density under constant solar and geomagnetic forcing. We examined longitudinal variation by plotting variables at a fixed local time over a period of several days. Figure 12 shows TIE-GCM

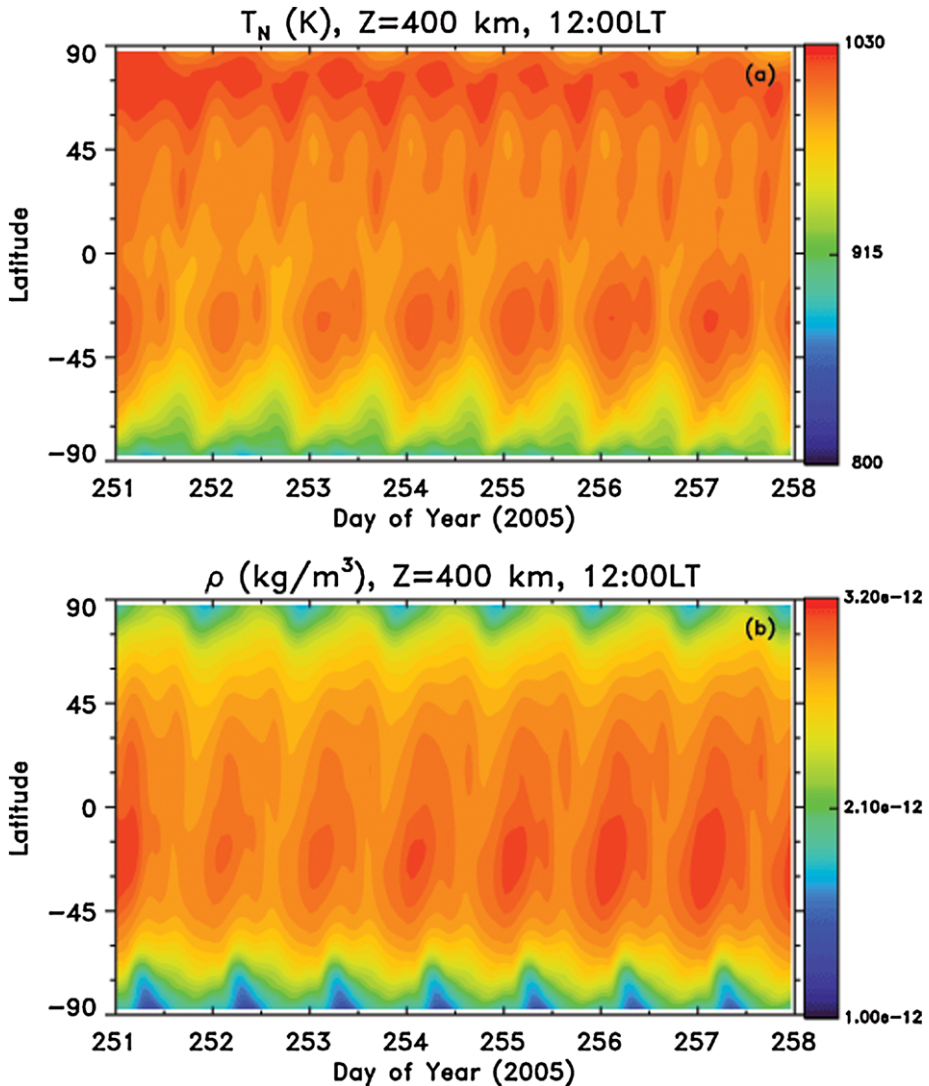


Fig. 12 Longitudinal variation of neutral temperature and neutral density. (a) TIE-GCM simulated neutral temperature at 400 km, 12:00LT, from day 251 to day 257 of 2005. (b) TIE-GCM simulated neutral density at 400 km, 12:00LT, from day 251 to day 257 of 2005

simulated neutral temperature and neutral density at 400 km, 12:00LT, from 2005251 to the beginning of 2005258 (September 8, 2005–September 16, 2005), assuming a constant solar and geomagnetic forcing. The real solar and geomagnetic forcing changed quite significantly in this period. F10.7 index was 94 on 2005251 (September 8, 2005), but was more than 110 through most of the period. In addition, there were several X-class flares on September 8 and September 9. On the other hand, Ap index was 8 on September 8, 2005, but increased to 105 on September 11, 2005. If we ran the model using the real forcing, then the longitudinal variation would be undistinguishable due to the larger density changes driven by the solar and geomagnetic forcing. We looked at CHAMP density in this period, and longitu-

dinal variation is hard to discern due to the overwhelmingly larger density changes driven by the solar and geomagnetic forcing. In order to be able to show the longitudinal variation, we kept the solar and geomagnetic forcing to be the same as those on September 8, 2005 for the entire period. Both neutral temperature and neutral density show an apparent periodical variation, with amplitude $\sim 15\%$. Although the periodicity is one day, this is not the diurnal variation that we discussed in Sect. 3.3. The periodicity shown in Fig. 12 is purely a longitudinal variation. Diurnal variation of neutral density is primarily caused by diurnal variation of solar irradiance, whereas longitudinal variation of neutral density is likely due to displacement of the geomagnetic pole from the geophysical pole. It is well understood that this displacement of the two poles causes longitudinal variation in the ionosphere. Effect of this displacement on the thermosphere is not clear. Further investigations are needed to understand the possible connection between the displacement of the two poles and the longitudinal variations shown in Fig. 12. Since the ionosphere and thermosphere are closely coupled energetically and dynamically, it is likely that the longitudinal variation of energetics and dynamics, associated with longitudinal variations in electron density (conductance), Joule heating, and auroral heating, is the primary cause of the longitudinal variation in the thermosphere shown in Fig. 12.

In Sect. 3.2, we discussed the possible effect of nonmigrating tides on the diurnal variation of neutral density. The effect of nonmigrating tides can also cause longitudinal variation of neutral density. Forbes et al. (2009) analyzed CHAMP and GRACE neutral density data and found that in the low latitude band ($\pm 30^\circ$), significant longitude variability (e.g., ± 25 K maximum to minimum over the equator) in geomagnetically-quiet exosphere temperatures exists, due to a spectrum of diurnal and semidiurnal thermal tides that are excited in the troposphere and strongly influenced by the global land-sea distribution. However, as we mentioned in Sect. 2, the effect of nonmigrating tides is not considered in the TIE-GCM, therefore, the longitudinal variation shown in Fig. 12 does not include contribution of nonmigrating tides.

There is a significant difference between latitudinal dependence of the longitudinal variation of temperature (Fig. 12a) and latitudinal dependence of longitudinal variation of neutral density (Fig. 12b). We have discussed differences in latitudinal variations of neutral temperature, neutral density, and neutral composition in previous subsection. Figure 12 again demonstrates that latitudinal gradient of composition, driven by different effect of circulations on lighter species O and heavier species N_2 , compensates the latitudinal gradient of neutral temperature, and thus causes small latitudinal gradient in neutral density and its variability.

4 Summary

Determination and prediction of neutral density is critical for satellite operations including catalog maintenance, collision avoidance, and reentry prediction. Neutral density is governed by thermospheric external forcing, internal neutral dynamics, thermosphere and ionosphere coupling, and effects from the lower and middle atmosphere. The primary forcing for the thermosphere is solar irradiance (< 175 nm). The secondary energy input for the thermosphere is geomagnetic activity through Joule heating and energetic particle precipitation. In addition to these two main external forcing, tides and waves propagating through the mesopause region provide significant forcing for the thermosphere. Variability in the external forcing, internal dynamics, and thermosphere and ionosphere coupling, drives complex density variation. This paper discussed temporal variations from abrupt changes to long-term trends, as well as spatial variations with latitude, longitude, and altitude. A summary

of these variations, their amplitude (at ~ 400 km), and their driving forcing mechanisms are as follows:

- Abrupt changes (minutes to hours): driven by solar flares and geomagnetic storms (associated with CME and/or flares). A large (X17) centrally located solar flare can cause ~ 30 – 40% density enhancement on the day side. The flare response in neutral density can be best observed on the dayside at low to mid-latitudes. A large geomagnetic storm ($Kp = 9$) can cause density enhancement on the order of ~ 100 – 200% . Storm response is largest at high latitudes.
- Diurnal variation: driven by presence and absence of solar irradiance during day and night, and the effects of middle-atmosphere tides. The amplitude of the diurnal variation is on the order of $\sim 100\%$.
- Multi-day variation: primarily driven by multi-day recurrent geomagnetic forcing associated with CIRs. The amplitude of the multi-day variation of density is on the order of ~ 30 – 50% .
- Solar-rotational variation: driven by the appearance and disappearance of the Sun's active regions as the Sun rotates in an average 27-day period. Solar-rotational variation is on the order of $\sim 100\%$ for high solar activity and decreases for lower solar activity.
- Annual/semiannual variation: driven by the annual variation of the Sun–Earth distance, semi-annual variation of inter-hemispheric large-scale circulation, semi-annual variation of geomagnetic activity, and likely lower atmospheric forcing through eddy diffusivity. The amplitude from annual minimum (\sim July) to annual maximum (equinoxes) is on the order of $\sim 100\%$, but with strong inter-annual variability from $\sim 30\%$ to $\sim 250\%$.
- Solar-cycle variation: driven by the intrinsic ~ 11 -year variability of magnetic activity in the Sun. The amplitude of the solar-cycle variation is about one order of magnitude.
- Long-term trends: primarily driven by global cooling in the upper atmosphere due to increasing concentration of CO_2 . The long-term trend of neutral density is approximately $-1.7\%/decade$ to $-3.0\%/decade$ for the past several decades.
- Latitudinal variation: driven by changes of solar irradiance in the two hemispheres associated with seasonal solar zenith angle changes, geomagnetic heating at high latitude, and internal dynamics. Neutral density shows little latitudinal variation during equinox seasons and $\sim 40\%$ increase from the winter pole to the summer pole.
- Longitudinal variation: likely driven by longitudinal variation of energetics and dynamics through thermosphere and ionosphere coupling, associated with longitudinal variations in electron density (conductance), Joule heating, and auroral heating. Amplitude of the longitudinal variation is on the order of $\sim 15\%$. This result is from the model simulations that did not include nonmigrating tides effect. Nonmigrating tides may introduce additional longitudinal variation.
- Variation with altitude: on a global mean basis, the thermosphere is in diffusive equilibrium state; therefore, thermospheric neutral density decreases exponentially with increasing altitude, according to the diffusive equilibrium density scale height, which is determined by temperature and composition.

Understanding neutral density, its variability, and driving mechanisms provide the means to continually improve operational neutral density models for satellite operations. We have gained significant knowledge through observational and modeling studies as summarized and discussed in this paper. Examples of remaining challenges are to quantify the temporal and spatial characteristics of rapid density changes in relation to the characteristics of the solar flares and geomagnetic disturbances that drive them, to investigate how lower/middle atmosphere forcing contributes to the annual/semiannual variation of neutral density, and

to determine whether the longitudinal variation of neutral density is due to magnetic field asymmetries affecting the ionosphere through thermosphere and ionosphere coupling.

Acknowledgements This research was supported by AFOSR contract FA9550-08-C0046 and NASA grants NNX08AQ31G, NNX10AF21G, and NNX07AC61G to the National Center for Atmospheric Research. NCAR is supported by the National Science Foundation. University of Colorado in Boulder supplied the CHAMP neutral density data that we used in this paper (<http://sisko.colorado.edu/sutton/data.html>). Bruce Bowman from the Air Force Space Command and John Emmert from the Naval Research Laboratory supplied the neutral density data at individual satellite perigees and global-mean neutral density data, respectively.

References

- B.R. Bowman, The semiannual thermosphere density variation from 1970 to 2002 between 200–1100 km, AAS 2004-174, in *AAS/AIAA Spaceflight Mechanics Meeting*, Maui, Hawaii, 8–12 February (2004)
- B.R. Bowman, F.A. Marcos, M. Kendra, A method for computing accurate daily atmospheric density values from satellite drag data, AAS 2004-173, in *AAS/AIAA Spaceflight Mechanics Meeting*, Maui, Hawaii, 8–12 February (2004)
- B.R. Bowman, W.K. Tobiska, F.A. Marcos, C. Valladares, The JB2006 empirical thermospheric density model. *J. Atmos. Sol.-Terr. Phys.* **70**, 774–793 (2007). doi:[10.1016/j.jastp.2007.10.002](https://doi.org/10.1016/j.jastp.2007.10.002)
- B.R. Bowman et al., The thermospheric semiannual density response to solar EUV heating. *J. Atmos. Sol.-Terr. Phys.* (2008). doi:[10.1016/j.jastp.2008.04.020](https://doi.org/10.1016/j.jastp.2008.04.020)
- S. Bruinsma, J.M. Forbes, R.S. Nerem, X. Zhang, Thermosphere density response to the 20–21 November 2003 solar and geomagnetic storm from CHAM and GRACE accelerometer data. *J. Geophys. Res.* **111**, A06303 (2006). doi:[10.1029/2005JA011284](https://doi.org/10.1029/2005JA011284)
- A.G. Burns, T.L. Killeen, W. Wang, R.G. Roble, The solar-cycle-dependent response of the thermosphere to geomagnetic storms. *J. Atmos. Sol.-Terr. Phys.* **66**, 14 (2004)
- P.C. Chamberlin, T.N. Woods, F.G. Eparvier, Flare Irradiance Spectral Model (FISM): Flare component algorithms and results. *Space Weather* **6**, S05001 (2008). doi:[10.1029/2007SW000372](https://doi.org/10.1029/2007SW000372)
- R.R. Clark, M.D. Burrage, S.J. Franke, A.H. Mansond, C.E. Meek, N.J. Mitchell, H.G. Muller, Observations of 7-d planetary waves with MLT radars and the UARS-HRDI instrument. *J. Atmos. Sol.-Terr. Phys.* **64**, 1217–1228 (2002)
- K. Davies, *Ionospheric Radio* (Peter Peregrinus, London, 1990)
- Y. Deng, T.J. Fuller-Rowell, R.A. Akmaev, A.J. Ridley, Impact of the altitudinal Joule heating distribution on the thermosphere. *J. Geophys. Res.* (2010, submitted)
- T.R. Detman, Cross validation comparisons of autonomous Ap predictions, in *Proceedings of Workshop on the Evaluation of Space Weather Forecasts*, ed. by K. Doggett (1996), p. 149, NOAA, ERL, Boulder, Colo
- B.A. Emery, I.G. Richardson, D.S. Evans, F.J. Rich, Solar wind structure sources and periodicities of auroral electron power over three solar cycles. *J. Atmos. Sol.-Terr. Phys.* **71** (2009). doi:[10.1016/j.jastp.2008.08.005](https://doi.org/10.1016/j.jastp.2008.08.005)
- J.T. Emmert, J.M. Picone, J.L. Lean, S.H. Knowles, Global change in the thermosphere: compelling evidence of a secular decrease in density. *J. Geophys. Res.* **109**, A02301 (2004)
- J.T. Emmert, J.M. Picone, R.R. Meier, Thermospheric global average density trends 1967–2007, derived from orbits of 5000 near-Earth objects. *Geophys. Res. Lett.* **35**, L05101 (2008). doi:[10.1029/2007GL032809](https://doi.org/10.1029/2007GL032809)
- J.T. Emmert, A long-term data set of globally averaged thermospheric total mass density. *J. Geophys. Res.* **114**, A06315 (2009). doi:[10.1029/2009JA014102](https://doi.org/10.1029/2009JA014102)
- J.T. Emmert, J.L. Lean, J.M. Picone, Record-low thermospheric density during the 2008 solar minimum. *Geophys. Res. Lett.* **37**, L12102 (2010). doi:[10.1029/2010GL043671](https://doi.org/10.1029/2010GL043671)
- J.T. Emmert, J.M. Picone, Climatology of globally averaged thermospheric mass density. *J. Geophys. Res.* **115**, A09326 (2010). doi:[10.1029/2010JA015298](https://doi.org/10.1029/2010JA015298)
- J.M. Forbes, S.L. Bruinsma, X. Zhang, J. Oberheide, Surface-exosphere coupling due to thermal tides. *Geophys. Res. Lett.* **36**, L15812 (2009). doi:[10.1029/2009GL038748](https://doi.org/10.1029/2009GL038748)
- J.M. Forbes, X. Zhang, E.R. Talaat, W. Ward, Nonmigrating diurnal tides in the thermosphere. *J. Geophys. Res.* **A108**(1), 1033 (2003). doi:[10.1029/2002JA009262](https://doi.org/10.1029/2002JA009262)
- T.J. Fuller-Rowell, The “thermospheric spoon”: A mechanism for the semiannual density variation. *J. Geophys. Res.* **103**, 3951–3956 (1998)
- M.E. Hagan, C. McLandress, J.M. Forbes, Diurnal tidal variability in the upper mesosphere and lower thermosphere. *Ann. Geophys.* **15**, 1176–1186 (1997). doi:[10.1007/s00585-997-1176-x](https://doi.org/10.1007/s00585-997-1176-x)

- M.E. Hagan, J.M. Forbes, Migrating and nonmigrating diurnal tides in the middle and upper atmosphere excited by tropospheric latent heat release. *J. Geophys. Res. D* **107**(24), 4754 (2002). doi:[10.1029/2001JD001236](https://doi.org/10.1029/2001JD001236)
- M.E. Hagan, J.M. Forbes, Migrating and nonmigrating semidiurnal tides in the upper atmosphere excited by tropospheric latent heat release. *J. Geophys. Res. A* **108**(2), 1062 (2003). doi:[10.1029/2002JA009466](https://doi.org/10.1029/2002JA009466)
- A.E. Hedín, Extension of the MSIS thermosphere model into the middle and lower atmosphere. *J. Geophys. Res.* **96**, 1159–1172 (1991)
- R.A. Heelis, J.K. Lowell, R.W. Spiro, A model of the highlatitude ionospheric convection pattern. *J. Geophys. Res.* **87**, 6339–6345 (1982)
- L.G. Jacchia, Static diffusion models of the upper atmosphere with empirical temperature profiles. *Smithson. Contrib. Astrophys.* **8**, 215–257 (1965)
- L.G. Jacchia, Semiannual variation in the heterosphere: A reappraisal. *J. Geophys. Res.* **76**, 4602–4607 (1971)
- C. Jacobi, R. Schminder, D. Kürschner, Planetary-wave activity obtained from long-period (2–18 days) variations of mesopause region winds over Central Europe (52°N, 15°E). *J. Atmos. Sol.-Terr. Phys.* **60**(1), 81–93 (1998)
- G.M. Keating, E.J. Prior, The winter He bulge. *Space Res.* **8**, 982 (1968)
- G.M. Keating, R.H. Tolson, M.S. Bradford, Evidence of long-term global decline in the Earth's thermospheric densities apparently related to anthropogenic effects. *Geophys. Res. Lett.* **27**, 1523–1526 (2000)
- D.J. Knipp, W.K. Tobiska, B.A. Emery, Direct and indirect thermosphere heating sources for solar cycle 21–23. *Sol. Phys.* **224**, 495–505 (2004)
- J. Laštovička, R.A. Akmaev, G. Beig, J. Bremer, J.T. Emmert, Global change in the upper atmosphere. *Science* **314**, 1253–1254 (2006)
- J.L. Lean, J.T. Emmert, J.M. Picone, R.R. Meier, Global and regional trends in ionospheric total electron content. *J. Geophys. Res.* **116**, A00H04 (2011). doi:[10.1029/2010JA016378](https://doi.org/10.1029/2010JA016378)
- J. Lei, J.P. Thayer, J.M. Forbes, E.K. Sutton, R.S. Nerem, Rotating solar coronal holes and periodic modulation of the upper atmosphere. *Geophys. Res. Lett.* **35**, L10109 (2008). doi:[10.1029/2008GL033875](https://doi.org/10.1029/2008GL033875)
- H. Liu, H. Lühr, Strong disturbance of the upper thermospheric density due to magnetic storms: CHAMP observations. *J. Geophys. Res.* **110**, A09S29 (2005). doi:[10.1029/2004JA010908](https://doi.org/10.1029/2004JA010908)
- H. Liu, H. Lühr, S. Watanabe, W. Köhler, C. Manoj, Contrasting behavior of the thermosphere and ionosphere in response to the 28 October 2003 solar flare. *J. Geophys. Res.* **112**, A07305 (2007a). doi:[10.1029/2007JA012313](https://doi.org/10.1029/2007JA012313)
- H. Liu, H. Lühr, S. Watanabe, Climatology of the equatorial thermospheric mass density anomaly. *J. Geophys. Res.* **112**, A05305 (2007b). doi:[10.1029/2006JA012199](https://doi.org/10.1029/2006JA012199)
- R. Liu, H. Lühr, E. Doornbos, S.-Y. Ma, Thermospheric mass density variations during geomagnetic storms and a prediction model based on the merging electric field. *Ann. Geophys.* **28**, 1633–1645 (2010). doi:[10.5194/angeo-28-1633-2010](https://doi.org/10.5194/angeo-28-1633-2010)
- R. Liu, S.-Y. Ma, H. Lühr, Predicting storm-time thermospheric mass density variations at CHAMP and GRACE altitudes. *Ann. Geophys.* **29**, 443–453 (2011). doi:[10.5194/angeo-29-443-2011](https://doi.org/10.5194/angeo-29-443-2011)
- H. Lühr, M. Rother, W. Köhler, P. Ritter, L. Grunwaldt, Thermospheric up-welling in the cusp region: Evidence from CHAMP observations. *Geophys. Res. Lett.* **31**, L06805 (2004). doi:[10.1029/2003GL019314](https://doi.org/10.1029/2003GL019314)
- F.A. Marcos, J.O. Wise, M.J. Kendra, N.J. Grossbard, B.R. Bowman, Detection of a long-term decrease in the thermospheric neutral density. *Geophys. Res. Lett.* **32**, L04103 (2005). doi:[10.1029/2004GL021269](https://doi.org/10.1029/2004GL021269)
- M. Mendillo et al., Behavior of the ionospheric F region during the great solar flare of August 7, 1972. *J. Geophys. Res.* **79**(4), 665–672 (1974)
- A.P. Mitra, *Ionospheric Effects of Solar Flares* (Reidel, Boston, 1974)
- S. Müller, H. Lühr, S. Rentz, Solar and magnetospheric forcing of the low latitude thermospheric mass density as observed by CHAMP. *Ann. Geophys.* **27**, 2087–2099 (2009)
- H.K. Paetzold, H. Zschörner, An annual and a semiannual variation of the upper air density. *Pure Appl. Geophys.* **48**, 85–92 (1961)
- D.J. Pawlowski, A.J. Ridley, Modeling the thermospheric response to solar flares. *J. Geophys. Res.* **113**, A10309 (2008). doi:[10.1029/2008JA013182](https://doi.org/10.1029/2008JA013182)
- J.M. Picone, A.E. Hedín, D.P. Drob, A.C. Aikin, NRLMSISE-00 empirical model of the atmosphere: Statistical comparisons and scientific issues. *J. Geophys. Res. A* **107**(12), 1468 (2002). doi:[10.1029/2002JA009430](https://doi.org/10.1029/2002JA009430)
- G.W. Pröls, Density perturbations in the upper atmosphere caused by the dissipation of solar wind energy. *Surv. Geophys.* **32**, 101–195 (2011). doi:[10.1007/s10712-010-9104-0](https://doi.org/10.1007/s10712-010-9104-0)
- L. Qian, R.G. Roble, S.C. Solomon, T.J. Kane, Calculated and observed climate change in the thermosphere, and a prediction for solar cycle 24. *Geophys. Res. Lett.* **33**, L23705 (2006). doi:[10.1029/2006GL027185](https://doi.org/10.1029/2006GL027185)

- L. Qian, S.C. Solomon, R.G. Roble, B.R. Bowman, F.A. Marcos, Thermospheric neutral density response to solar forcing. *Adv. Space Res.* **42**(5), 926–932 (2008). doi:[10.1016/j.asr.2007.10.019](https://doi.org/10.1016/j.asr.2007.10.019)
- L. Qian, S.C. Solomon, T.J. Kane, Seasonal variation of thermospheric density and composition. *J. Geophys. Res.* **114**, A01312 (2009). doi:[10.1029/2008JA013643](https://doi.org/10.1029/2008JA013643)
- L. Qian, A.G. Burns, P.C. Chamberlin, S.C. Solomon, Flare location on the solar disk: Modeling the thermosphere and ionosphere response. *J. Geophys. Res.* **115**, A09311 (2010a). doi:[10.1029/2009JA015225](https://doi.org/10.1029/2009JA015225)
- L. Qian, S.C. Solomon, M.G. Mlynczak, Model simulation of thermospheric response to recurrent geomagnetic forcing. *J. Geophys. Res.* **115**, A10301 (2010b). doi:[10.1029/2010JA015309](https://doi.org/10.1029/2010JA015309)
- L. Qian, A.G. Burns, P.C. Chamberlin, S.C. Solomon, Variability of thermosphere and ionosphere responses to solar flares. *J. Geophys. Res.* (2011, accepted)
- C.A. Reber, J.E. Cooley, D.N. Harpold, Upper atmosphere hydrogen and helium measurements from the Explorer 32 satellite. *Space Res.* **8**, 993 (1968)
- C. Reigber, H. Lühr, P. Schwintzer, CHAMP mission status. *Adv. Space Res.* **30**(2), 129–134 (2002)
- P.G. Richards, J.A. Fennelly, D.G. Torr, EUVAC: A solar EUV flux model for aeronomic calculations. *J. Geophys. Res.* **99**, 8981–8992 (1994)
- A.D. Richmond, E.C. Ridley, R.G. Roble, A thermosphere/ionosphere general circulation model with coupled electrodynamics. *Geophys. Res. Lett.* **19**, 601–604 (1992)
- H. Rishbeth, A greenhouse effect in the ionosphere? *Planet. Space Sci.* **38**, 945–948 (1990)
- H. Rishbeth, R.G. Roble, Cooling of the upper atmosphere by enhanced greenhouse gases—modelling of thermospheric and ionospheric effects. *Planet. Space Sci.* **40**, 1011–1026 (1992)
- R.G. Roble, E.C. Ridley, An auroral model for the NCAR thermosphere general circulation model (TGCM). *Ann. Geophys. A* **5**(6), 369–382 (1987)
- R.G. Roble, E.C. Ridley, A.D. Richmond, R.E. Dickinson, A coupled thermosphere/ionosphere general circulation model. *Geophys. Res. Lett.* **15**, 1325 (1988). doi:[10.1029/GL015i012p01325](https://doi.org/10.1029/GL015i012p01325)
- R.G. Roble, R.E. Dickinson, How will changes in carbon dioxide and methane modify the mean structure of the mesosphere and lower thermosphere? *Geophys. Res. Lett.* **16**, 1441–1444 (1989)
- C.T. Russell, R.L. McPherron, Semiannual variation of geomagnetic activity. *J. Geophys. Res.* **78**, (1), 92–108 (1973)
- S.C. Solomon, L. Qian, Solar extreme-ultraviolet irradiance for general circulation models. *J. Geophys. Res.* **110**, A10306 (2005). doi:[10.1029/2005JA011160](https://doi.org/10.1029/2005JA011160)
- S.C. Solomon, T.N. Woods, L.V. Didkovsky, J.T. Emmert, L. Qian, Anomalously low solar extreme-ultraviolet irradiance and thermospheric density during solar minimum. *Geophys. Res. Lett.* **37**, L16103 (2010). doi:[10.1029/2010GL044468](https://doi.org/10.1029/2010GL044468)
- S.C. Solomon, L. Qian, L.V. Didkovsky, R.A. Viereck, T.N. Woods, Causes of low thermospheric density during the 2007–2009 solar minimum. *J. Geophys. Res.* **116** (2011). doi:[10.1029/2011JA016508](https://doi.org/10.1029/2011JA016508)
- E.K. Sutton, J.M. Forbes, R.S. Nerem, Global thermospheric neutral density and wind response to the severe 2003 geomagnetic storms from CHAMP accelerometer data. *J. Geophys. Res.* **110**, A09S40 (2005). doi:[10.1029/2004JA010985](https://doi.org/10.1029/2004JA010985)
- M. Temmer, B. Vrsnak, A.M. Veronig, Periodic appearance of coronal holes and the related variation of solar wind parameters. *Sol. Phys.* **241**, 371–383 (2007)
- B.T. Tsurutani, W.D. Gonzalez, A.L.C. Gonzalez, F. Tang, J.K. Arballo, M. Okada, Interplanetary origin of geomagnetic activity in the declining phase of the solar cycle. *J. Geophys. Res. A* **100**(11), 21717–21733 (1995)
- B.T. Tsurutani et al., Extreme solar EUV flares and ICMEs and resultant extreme ionospheric effects: comparison of the Halloween 2003 and the Bastille Day events. *Radio Sci.* **41**, RS5S07 (2006). doi:[10.1029/2005RS003331](https://doi.org/10.1029/2005RS003331)
- R.L. Walterscheid, The semiannual oscillation in the thermosphere as a conduction mode. *J. Geophys. Res.* **87**, 10527–10535 (1982)
- W. Wang, A.G. Burns, M. Wiltberger, S.C. Solomon, T.L. Killeen, Altitude variations of the horizontal thermospheric winds during geomagnetic storms. *J. Geophys. Res.* **113**, A02301 (2008). doi:[10.1029/2007JA012374](https://doi.org/10.1029/2007JA012374)
- G.R. Wilson, D.R. Weimer, J.O. Wise, F.A. Marcos, Response of the thermosphere to Joule heating and particle precipitation. *J. Geophys. Res.* **111**, A10314 (2006). doi:[10.1029/2005JA011274](https://doi.org/10.1029/2005JA011274)
- T.N. Woods, F.G. Eparvier, S.M. Bailey, P.C. Chamberlin, J. Lean, G.J. Rottman, S.C. Solomon, W.K. Tobiska, D.L. Woodraska, Solar EUV Experiment (SEE): Mission overview and first results. *J. Geophys. Res.* **110**, A01312 (2005). doi:[10.1029/2004JA010765](https://doi.org/10.1029/2004JA010765)
- D.H. Zhang, Z. Xiao, Study of ionospheric response to the 4B flare on 28 October 2003 using International GPS Service network data. *J. Geophys. Res.* **110**, A03307 (2005). doi:[10.1029/2004JA010738](https://doi.org/10.1029/2004JA010738)
- D.H. Zhang, X.H. Mo, L. Cai, W. Zhang, M. Feng, Y.Q. Hao, Z. Xiao, Impact factor for the ionospheric total electron content response to solar flare irradiation. *J. Geophys. Res.* **116**, A04311 (2011). doi:[10.1029/2010JA016089](https://doi.org/10.1029/2010JA016089)